Chinese Journal of Chemical Physics
化学物理学报

Volume 39, Issue 3
June 2026

A Novel Raman Spectrometer using Bessel-like Laser Beam for Homogeneous Phases and Interface Detections

Ning Chen, Yuhui Li, Tianle Zhang, Jin Yang, Xiaoguo Zhou*, Shilin Liu*

Chin. J. Chem. Phys. **39**, 318–327 (2026)

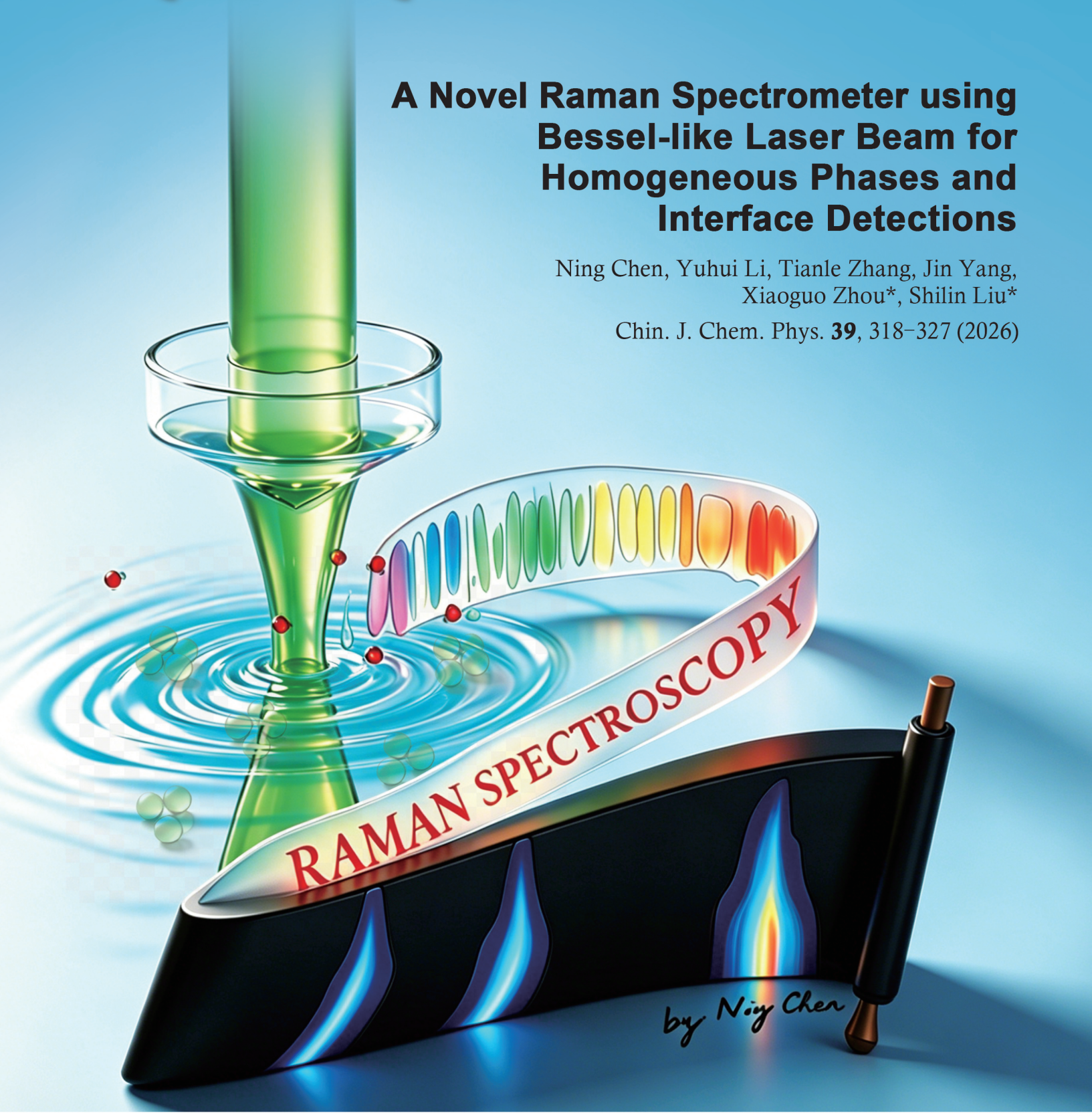

Chinese Physical Society
中国物理学会
AIP Publishing

ARTICLE

A Novel Raman Spectrometer using Bessel-like Laser Beam for Homogeneous Phases and Interface Detections

Ning Chen, Yuhui Li, Tianle Zhang, Jin Yang, Xiaoguo Zhou*, Shilin Liu*

Hefei National Research Center for Physical Sciences at the Microscale, Department of Chemical Physics, University of Science and Technology of China, Hefei 230026, China

(Dated: Received on February 1, 2025; Accepted on March 7, 2025)

Bessel beams, often referred to as "non-diffractive" light, have been successfully applied in numerous fields. In this study, we integrated a Bessel beam as the illumination source into a Raman spectrometer to enhance the detection of homogeneous phases and interfaces. By simulating optical path systems, we optimized the setup to fully utilize the multi-pixel array and maximize detection sensitivity. Compared to a conventional Gaussian-beam Raman spectrometer in the 90°-scattered configuration, the upgraded Raman spectrometer employing a Bessel-like beam demonstrated a nearly 6-fold improvement in sensitivity. Additionally, it significantly suppressed background scattering interferences in the low-frequency range, thus enhancing the clarity and accuracy of spectral data. Furthermore, the capability of this spectrometer for real-space Raman imaging of heterogeneous phase interfaces was verified. This advancement not only improves the sensitivity and precision of Raman measurements but also expands the potential applications of Raman spectroscopy in studying complex systems, such as interfaces and phase boundaries, with high spatial and spectral resolution.

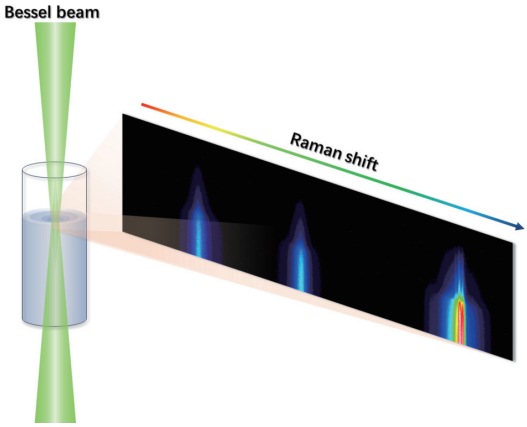

Key words: Raman spectroscopy, Raman imaging, Interface, Bessel beam, Gaussian beam

I. INTRODUCTION

Raman spectroscopy is one of the most powerful techniques for molecular identification, leveraging specific vibrational fingerprints to characterize chemical species. Its non-destructive and label-free nature has made it a versatile tool across diverse fields, including materials science, combustion research, biochemistry, and more [1–5]. Compared to infrared spectroscopy, Raman spectroscopy offers distinct advantages, particularly when analyzing species in aqueous solutions. Vibrational peaks in Raman spectra are typically narrower, providing more detailed and resolved vibrational structures. This enhanced resolution makes Raman spectroscopy particularly valuable for studying complex molecular systems and dynamic processes in solution-phase environments.

A Raman spectrometer typically consists of a light source, optical system, sample holder, monochromator, and detector. Tight focusing of the incident light is essential due to the inherently small Raman scattering cross-sections, which also highlights the potential value of spatial resolution in Raman measurements. The resolution and detection limit of a commercial spectrometer are primarily determined by the monochromator and

* Authors to whom correspondence should be addressed.
E-mail: xzhou@ustc.edu.cn, slliu@ustc.edu.cn

detector, while the sample illumination system defines the phase of the material under investigation. Apart from micro-Raman systems that utilize microscopes, macro-Raman designs are widely employed in commercial spectrometers. In these systems, the scattered light collection setup, which includes the monochromator and detector, is positioned at a 90° angle relative to the incident illumination. The collected Raman scattered light is dispersed by optical gratings within the monochromator in a direction perpendicular to the grating grooves and then detected by a photodetector. Over the past few decades, charge-coupled devices (CCDs) have become the gold standard for photodetectors in Raman spectrometers due to their high sensitivity and low noise ratios [6–8]. Their widespread adoption has significantly enhanced the performance of Raman spectroscopic measurements.

Notably, in this 90°-scattering configuration, the entrance slit of monochromator is typically set to a narrow width of a few hundred microns to ensure high energy resolution. In this setup, the collected Raman light along the direction parallel to the grating grooves of monochromator often does not fully utilize the grating or the multi-row pixels of the CCD detector. For example, when using a TEM00 incident laser, the imaging intensity of Raman scattered light on the CCD exhibits a typical Gaussian distribution along the direction parallel to the grooves. This configuration inevitably leads to underutilization of pixels in rows away from the center in the CCD detectors. To address this limitation and maximize the use of the two-dimensional array of CCD detectors, an asymmetrical spot profile for the incident illumination is required. By shaping the incident light to have an asymmetrical intensity distribution, the Raman scattered light can be more evenly distributed across the CCD, ensuring that more pixels are effectively utilized. This approach enhances the sensitivity and efficiency of the spectrometer, enabling better detection and analysis of Raman signals.

As depicted in FIG. 1(a), a simple strategy to achieve an asymmetrical light spot is to use a cylindrical lens. However, this approach suffers from a significant drawback: the uneven distribution of light intensity along the cylindrical direction. Additionally, while an ellipsoidal focus can be formed by using a spherical lens for a Gaussian laser beam, creating a naturally asymmetric illumination region near the focal point, this method also has limitations. When the entrance slit of

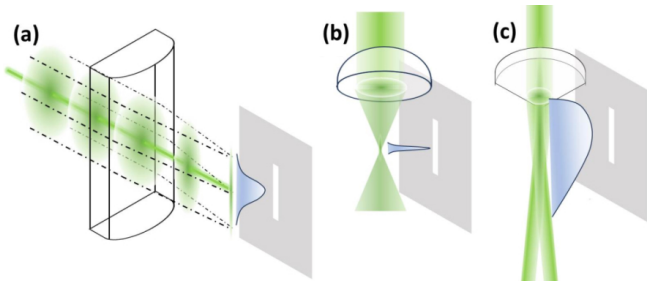

FIG. 1 Three common strategies to produce an asymmetrical spot of the incident illumination in Raman spectrometer using the grating monochromator and CCD detector, (a) use of cylindrical lens, (b) an ellipsoidal focus by using a spherical lens, (c) the extended linear focus of Bessel beam.

the monochromator is aligned parallel to the laser propagation direction (FIG. 1(b)), the limited confocal length (typically dozens of micrometers) is insufficient to match the size of the CCD detector. To address these challenges, the Bessel beam, a type of "non-diffracting beam" [9], emerges as the ideal candidate for upgrading the Raman spectrometer. The intensity distribution of a Bessel beam typically consists of a small central core surrounded by controllable ring spots. Importantly, this distribution remains unchanged over a relatively long distance along the direction of propagation. Compared to a Gaussian beam, the Bessel beam offers several advantages, including non-diffracting properties, long focal depth, and self-repairing capabilities. These features make it particularly well-suited for enhancing the sensitivity and spatial resolution of Raman spectroscopic measurements, enabling more efficient utilization of the CCD detector and improving overall system performance.

Although it is impossible to generate an ideal Bessel beam in a laboratory setting due to its requirement for infinite power, a close approximation to a zero-order Bessel beam can be easily achieved using an axicon. Owing to its distinctive advantages mentioned above, the Bessel-like beam has found successful applications in numerous fields, such as optical collimation and measurement [10, 11], laser micromachining [12, 13], optical tweezers [14, 15], biological imaging [16, 17] and laser-induced breakdown spectroscopy [18]. In the context of Raman spectroscopy, Ren *et al.* were the first to develop a Bessel beam-based Raman spectrometer for detecting drugs in scattering media, utilizing a 90°-scattering configuration [19, 20]. Subsequently, Fleming and his colleagues conducted another Bessel Raman spectrometer in a backscattered geometry, extending its ap-

DOI: 10.1063/1674-0068/cjcp2502011

plication to spatially offset Raman spectroscopy [21]. In these studies, the non-diffracting and self-repairing characteristics of the Bessel beam were emphasized.

In this study, we leveraged another key advantage of the Bessel beam: its extended linear focus region, which can span up to a few millimeters [22, 23]. This property allows for the creation of an asymmetrical spot in the incident illumination with ease. When focused, the beam waist of the incident illumination region is reduced to a few micrometers, while the focal depth extends to sub-millimeter scales. By aligning the monochromator slit parallel to the direction of incident light propagation, we developed a novel Raman spectrometer utilizing a Bessel-like laser beam. In this setup, the Raman scattering from the linear focus region is collected, dispersed and mapped onto the CCD detector. This configuration ensures that all pixels in the rows of the CCD detector are utilized with uniform efficiency, significantly enhancing the sensitivity and spatial resolution of the spectrometer.

In this upgraded configuration, the detected CCD image essentially represents a projection of the incident illumination region. This unique feature opens up another potential application scenario for this spectrometer: recording Raman images of heterogeneous phase interfaces, such as solid-liquid surface, or gas-liquid and liquid-liquid interfaces. Given the critical role interfaces play in numerous physical and chemical processes [24], advanced nonlinear spectroscopic techniques, such as sum frequency generation (SFG) and second harmonic generation (SHG) spectroscopy [24–29], surface-enhanced Raman (SER) spectroscopy [30–34], have been developed to achieve interface-sensitive detection. These techniques are highly sensitive to the nanometer-scale spatial extent of the interface region. However, in the case of heterogeneous diffusion, interfaces can extend to tens or even hundreds of microns, rendering the above nonlinear spectroscopic approaches less applicable. In contrast, we performed several proof-of-concept experiments to demonstrate the applicability of the upgraded spectrometer for interfacial detection, particularly at liquid-liquid diffusion interfaces. The extended linear focus region and uniform illumination of the Bessel beam enable the spectrometer to capture detailed Raman images of such interfaces, providing valuable insights into interfacial dynamics and molecular interactions over larger spatial scales.

II. RAMAN SPECTROMETER

A. Generation of Bessel-like laser beam

The incident illumination system is crucial for Raman imaging, especially its beam waist and the focal depth, which usually play a decisive role for spatial resolution and depth of detection. As the commercial laser is a Gaussian beam, we designed a new Bessel-based optical system including two axicons and one plano-convex lens, as displayed in FIG. 2(a). Compared with the single-axicon system, the double-axicon design has more application flexibility. The appropriate composition and relative distances among all optical elements were determined through the simulation using the Zemax software.

A TEM_{00} Gaussian beam from a CW laser (Coherent, Verdi V5, 532 nm) is converted to a Bessel-like beam after the first axicon (Thorlabs, AX122M-A, physical angle 2.0°). The image of energy distribution recorded with a camera beam profiler (Thorlabs, BC106N-VIS/M) exhibits a small central core and over 10 rings just behind the axicon, in line with the characteristics of the Bessel-like beam. Then, a collimated non-diffractive beam is formed after the second identical axicon placed at 300 mm downstream. As indicated in the image, the collimated beam involves a bright central spot and a series of rings. The experimentally measured spot size and energy distribution are also consistent with the simulated results. Moreover, thanks to its collimated and non-diffractive features, the beam can propagate for a long distance, therefore, it is convenient to be combined into a Raman spectrometer as the excitation light source.

A doublet lens (focal length f=50 mm) was placed in front of the sample cuvette to improve the power density of incident laser. Based on our optical simulations, a linearly focused zone is produced, where the power density along the light propagation is submillimeter-sized and the focused beam waist is about 3.4 microns. Although the laser spot size at the focal plane is too small to be distinctly detected by our camera beam profiler (FIG. 2(b)), the focused Bessel-like beam is undoubted. In addition, more than 85% of the incident laser power is retained in the focused Bessel-like beam.

B. Optical system for collecting Raman scattering light

As mentioned above, an approximately cylindrical il-

DOI: 10.1063/1674-0068/cjcp2502011

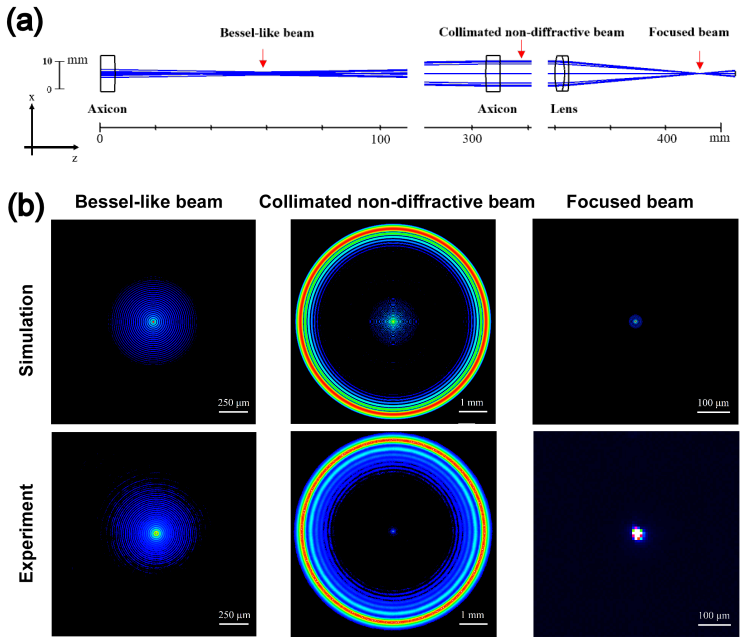

FIG. 2 (a) Diagram of the simulated Bessel-like beam generating optical path with an incident Gaussian laser beam; (b) simulated (upper panel) and experimental (bottom panel) energy distributions of the Bessel beam along the direction of laser propagation, where the positions of these three images from left to right were noted with red arrows in (a).

luminant is achieved as the excitation light source according to the application of the Bessel-like laser beam. To aim at the maximal collection efficiency on the basis of the F-number of monochromator (Acton Research, TriplePro), a special telescope was adopted to map Raman images of the detected region. As shown in FIG. 3, an aspherical lens (50.8-mm diameter, focal length $f=40$ mm) and an achromatic doublet lenses (50.8-mm diameter, focal length $f=200$ mm) make up core components of our optical system for collecting Raman scattered light. The distance between the illuminant and the aspherical lens is fixed at 40 mm, to collect scattered light at a relatively large solid angle. The collimated light is then focused into the monochromator slit (labelled with a line in FIG. 3) by the doublet lens, where chromatic and spherical aberrations are minimized. The distance between the aspherical lens and doublet lenses is flexible in a large range, and in the current study it has been set to be 150 mm.

According to the optical simulation in FIG. 3, the image of the cylindrical illuminant (4 μm-diameter and 400 μm-generatrix) is projected onto the preset focal plane with minimal aberrations. Thus, when the monochromator slit is placed at the focal position and parallel to the generatrix of the cylinder (the x-axis in FIG. 3), the Raman image of the cylindrical radiator is recorded with an approximate magnification factor of 5.

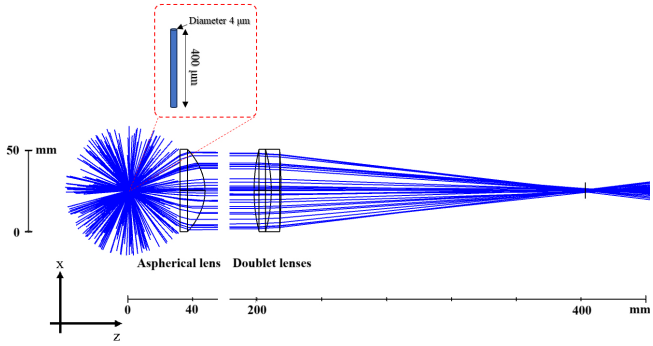

FIG. 3 Simulation of the optical path for collecting Raman scattered light from a cylindrical illuminant.

C. Monochromator and detector

FIG. 4 shows a schematic diagram of the assembled configuration of the current Raman spectrometer. To map the Raman image of a whole detected region, the orientations of the incident light, the collection optical path, the monochromator slit, and the CCD detector need to match each other. In the current experiments, the incident light is oriented vertically in experiments, and the collecting optical path and the monochromator are placed on the horizontal plane.

A cylindrical quartz cuvette (8-mm inner diameter and 35-mm height) was designed to hold samples in gas and liquid phases. The cuvette allows the incident laser to pass through from top to bottom, and its inner diameter is sufficiently large compared to the focused laser spot. After being dispersed by the gratings in the

DOI: 10.1063/1674-0068/cjcp2502011

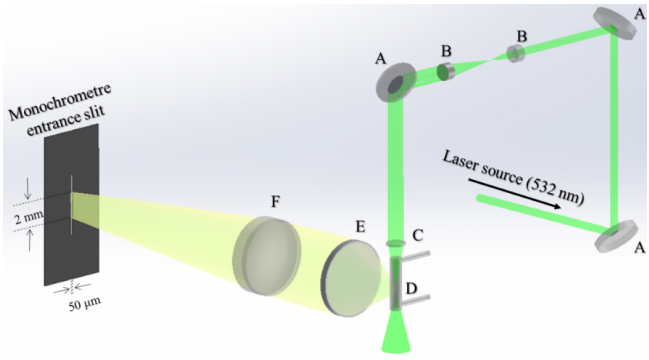

FIG. 4 Schematic diagram of the assembled configuration of the current Raman spectrometer, where A is the high reflectivity dielectric mirror, B is the axicon, C is the doublet lens, D is the sample cuvette, E is an aspherical lens, and F is an achromatic doublet lens.

monochromator, the Raman scattered light is projected onto a liquid-nitrogen-cooled CCD detector (Princeton Instrument, Spec-10:100B). This detector features back-illuminated, deep-depletion CCD with a 1340×100 pixel array, where each pixel measures 20 μm squared. Notably, the entire CCD imaging area spans 26.8 mm (horizontally) × 2.0 mm (vertically). When the entrance slit width of the monochromator is set to 50 μm, the corresponding incident illumination region measures 10 μm (horizontally) × 400 μm (vertically). This height is generally sufficient to capture Raman images of the interface region.

III. RESULTS AND DISCUSSION

A. Uniformity and sensitivity of CCD imaging

When the two-dimensional array of CCD is used, the uniformity of the CCD image is essential for resolution and sensitivity of a Raman imaging spectrometer. FIG. 5 (a) and (b) show the recorded Raman images of liquid CCl_4 using the Gaussian beam and Bessel-like beam, respectively. Notably, a 90-degree-scattered optical system was used for the Raman spectrometer using an incident Gaussian beam, whose details are described in Supplementary materials (SM). In the current frequency range, three vibrational peaks are observed, *i.e.* the peaks at 218 cm^{-1} and 315 cm^{-1} are contributed by the antisymmetric stretching vibration, while the peak at 459 cm^{-1} with maximal intensity is attributed to the symmetric stretching vibration. By integrating the signal distributions along the y-axis at each specific x-axis pixel, Raman spectra of CCl_4 were achieved and displayed in FIG. 5(c).

As shown in FIG. 5(a), only central region of the CCD is lightened using the Gaussian beam, confirming the moderate waste of CCD pixels. Moreover, a Gaussian-like intensity distribution along the y-axis is recorded with the FWHM of 13.4 pixels (corresponding to 268 μm), as shown in FIG. 5(e). Thus, the detected size of the scattering region (268/5 = 53.6 μm) is much larger than the waist of the Gaussian beam, indicating the moderate diffraction effects.

When the Bessel beam was employed, three bright lines were observed on the CCD image instead of spots, corresponding to the three vibrational peaks. The absolute brightness of these lines is consistently weaker than that with the Gaussian beam (FIG. 5 (a) and (b)), due to the lower power density of the incident laser beam on the focal plane as mentioned above. For example, at the pixel of 1151 corresponding to the maximal spectral intensity, the measured intensity using the Bessel beam is only 73.5% of that in the Gaussian mode (FIG. 5(e)), but the distribution along the vertical direction is uniform. By integrating all intensities along the y-axis, the measured Raman spectrum using the Bessel-like beam is plotted in FIG. 5(c), as well as that in the Gaussian beam mode. Apparently, in the same experimental conditions, such as the incident laser power (110 mW) and the integral time (500 ms), the Raman spectrum using the Bessel beam shows the completely identical vibrational structures with much stronger intensities (5.8-fold). In other words, the sensitivity of the Raman spectrometer is significantly improved, when introducing the Bessel-like laser beam.

The depolarization ratio (ρ) is an important parameter for determining the symmetry of vibrational modes, defined as $\rho = I_\perp / I_\parallel$, where $I_\perp$ and $I_\parallel$ represent the perpendicular and parallel scattered intensities relative to the plane of the incident polarized light. Typically, the scattered signal from spherical particles illuminated by a linearly polarized laser beam is completely linearly polarized ($\rho = 0$). To assess the impact of the Bessel-like beam on this parameter, we measured the depolarization ratios of three vibrational peaks of CCl_4 using both the Gaussian and Bessel beams. As shown in FIG. 5(d), the measured ρ values are entirely consistent between the two illumination modes. This result indicates that the introduction of the Bessel-like beam does not introduce any visible influence on the depolarization ratio, thus preserving the integrity of the polarization information in the Raman spectra.

DOI: 10.1063/1674-0068/cjcp2502011

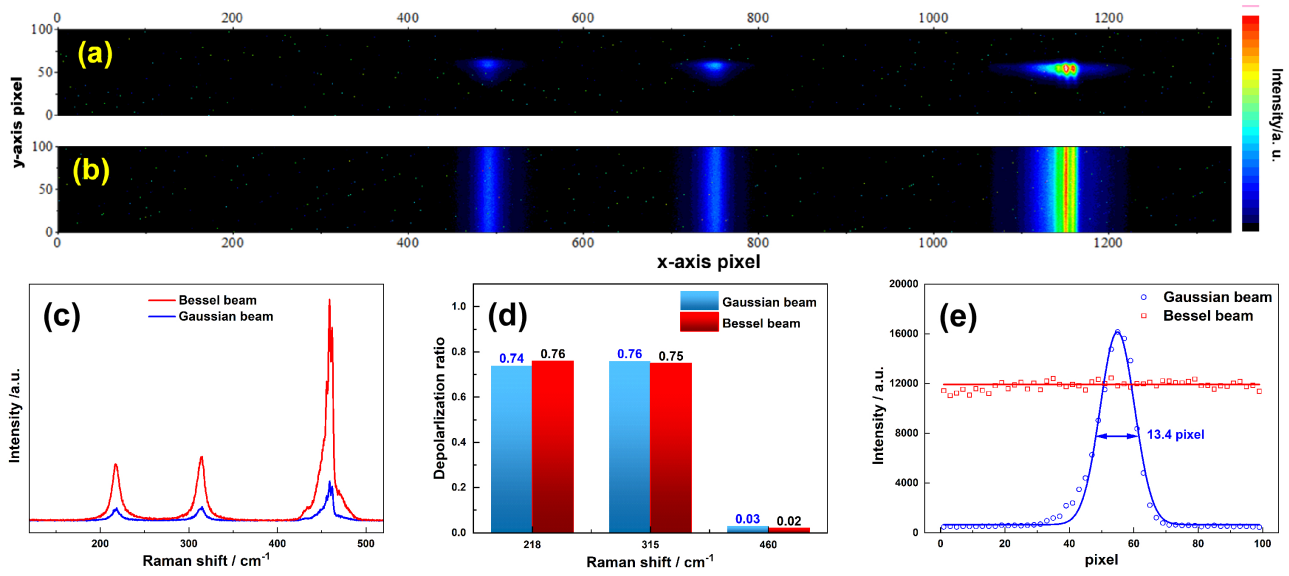

FIG. 5 CCD images (1340×100 pixels) of the Raman scattering of liquid CCl_4, with the Gaussian (a) and Bessel (b) laser beam as the excitation light source, as well as the corresponding Raman spectra (c), the measured depolarization ratios of the three peaks (d), and the intensity distributions along the vertical direction (100 pixel width) at the 1151 pixel of images (e) under the two experimental conditions, where the integral time (500 ms) and incident laser power (110 mW @ 532 nm) are the same.

B. Performance of the upgraded spectrometer on homogeneous solutions

To evaluate the performance of the upgraded spectrometer, we carried out several additional measurements on homogeneous liquids, including pure water and hen egg white lysozyme (HEWL) aqueous solution, using both Gaussian and Bessel-like laser beams at the identical power. The recorded Raman spectra in the frequency range of 450–1820 cm^{-1} are presented in FIG. 6.

As shown in FIG. 6, the peak positions and widths of the vibrational bands are very similar in the two conditions, except for the stronger intensities when applying the Bessel beam. In FIG. 6(a), an isolated Raman peak with the central position at 1635 cm^{-1} is well-known as the bending vibration of water, while the Raman spectrum of lysozyme in the range of 450–1820 cm^{-1} includes many known vibrational peaks of protein secondary and tertiary structures, *e.g.* the wide amide I band covering the range of 1620–1700 cm^{-1}, the N–C_α–C stretching vibration of HEWL skeleton at 933 cm^{-1}, the in-phase symmetric breathing vibration of phenyl ring of tryptophan (Trp) residues on lysozyme side chains at 759 cm^{-1}, the Trp Fermi resonance (so-called "W7" mode, located at 1340 and 1360 cm^{-1}), and the S–S stretching vibration peak of disulfide bonds at 507 cm^{-1}. Since the positions and widths of these peaks are very sensitive to ambient temperature or the conformation of the protein, we have successfully applied them as the indicators for phase-transitions of water [35] and transformations of protein structures [36–40].

In particular, the relative intensities of the vibrational peaks in the low and high-frequency ranges of FIG. 6 show noticeable variations between the two conditions (Gaussian and Bessel-like beams), regardless of whether it is pure water and lysozyme aqueous solution. When the relative intensities in the higher frequency range are normalized for both conditions (the grey and red curves in FIG. 6), the baseline in the lower frequency range for the Gaussian mode is significantly higher and exhibits an exponential decrease with increasing frequency. The elevated baseline in the Gaussian mode is likely due to residual Rayleigh scattering or fluorescence from impurities. In contrast, the use of the Bessel beam efficiently suppresses background scattering in the low-frequency range.

C. Spatial resolution along the vertical direction

Spatial resolution is one of the most important parameters for Raman imaging, particularly in the detection of interfaces. Although achromatic doublet lenses are employed in the collection optical system, the recorded images are always susceptible to instrumental resolution, diffractions, optical path vibrations, and other factors. As a result, the acquired signal is efficient-

DOI: 10.1063/1674-0068/cjcp2502011

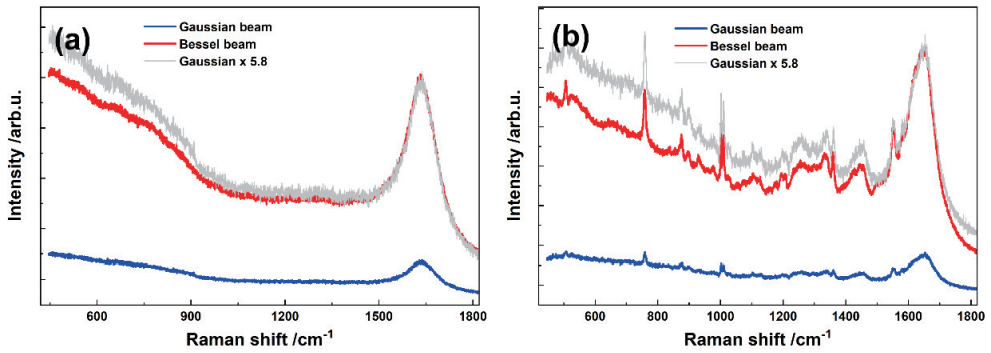

FIG. 6 Raman spectra of (a) water and (b) lysozyme aqueous solution, in which the blue traces were acquired with the Gaussian beam, and the red ones are the results using the Bessel beam. The integral time and incident laser power were identical in two experiments.

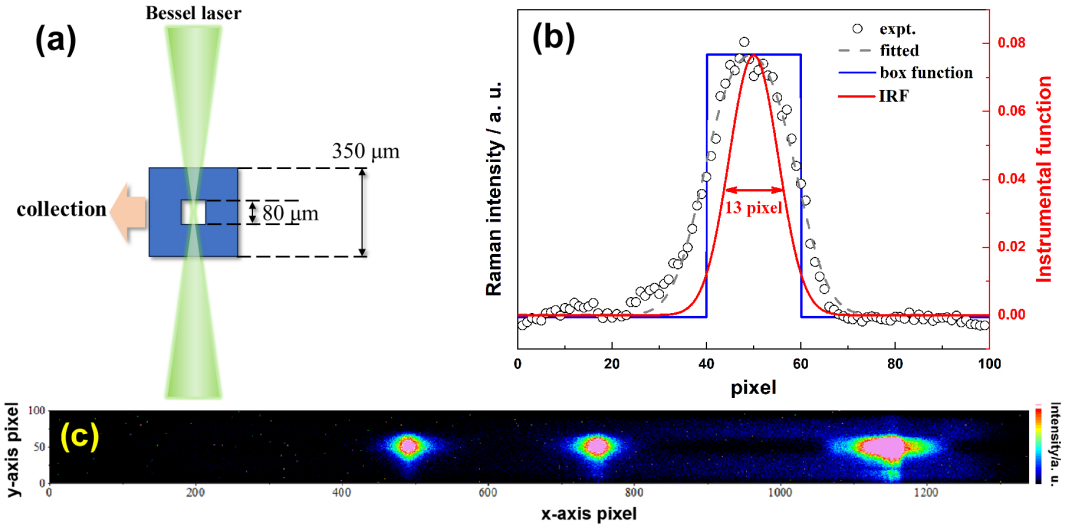

FIG. 7 (a) Schematic diagram of the quartz capillary tube and optical paths; (b) the intensity distributions along the vertical direction, where the red curve is the obtained instrumental resolution function including diffraction effects; (c) the recorded CCD image of CCl_4 in the capillary tube.

ly a convolution of the real signal and an instrumental resolution function (IRF). Thus, the IRF is extremely important for evaluating the spatial resolution of the instrument in Raman imaging mode. Typically, the IRF follows a Gaussian-type function.

A quartz capillary square tube with an inner length of 80 μm and a thickness of 135 μm was employed. When filled with liquid-phase CCl_4, this setup creates two ideal solid-liquid (Quartz-CCl_4) interfaces, as illustrated in FIG. 7(a). In this configuration, the Raman image of CCl_4 is expected to exhibit a box function along the direction perpendicular to the interface, assuming that diffraction effects are negligible. The box width is approximately 20 pixels, corresponding to 400 μm, that is 5 times the inner length of the tube. FIG. 7(c) displays the recorded CCD image, where the x-axis in pixels corresponds to the frequency range of 120–520 cm^{-1}. Similar to FIG. 5(a), three vibrational peaks are observed in the image. The intensity distribution along the vertical direction at the 1151 pixel position of image is exhibited in FIG. 7(b).

The measured intensity distribution of Raman scattering does not exhibit a perfect box-function shape due to diffraction effects, as shown in FIG. 7(b). To address this, we performed a deconvolution with a box function (20-pixel width) to extract the Gaussian-type instrumental resolution function, which is plotted in FIG. 7(b) as a red curve. The full-width at half-maximum (FWHM) of this Gaussian function is 13 pixel, indicating that the spatial resolution of interface-imaging using the current spectrometer is approximately 52 microns ((13 pixel × 20 μm/pixel)/5). Notably, this 13-pixel width aligns precisely with the width observed in FIG. 5(e), underscoring the significant role of diffraction effects in determining the spatial resolution of the current setup. While the current resolution may not be

DOI: 10.1063/1674-0068/cjcp2502011

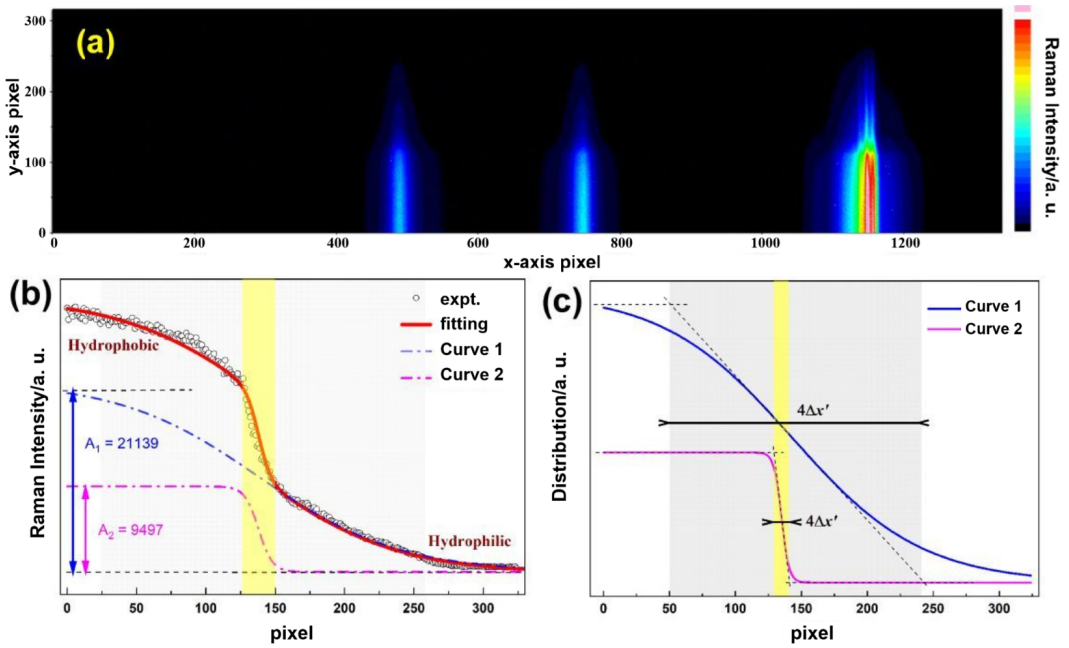

FIG. 8 (a) Raman image of the interface region of CCl_4/H_2O; (b) the image intensity distribution along the vertical direction at the 1151 pixel of the image, where the corresponding fitted curve with double Boltzmann sigmoidal functions is plotted in red; (c) the density distributions of the two components after deconvolution with IRF.

ideal for all applications, it is sufficient for Raman imaging of liquid-liquid diffusion interface region.

D. Raman imaging and spectroscopy of heterogeneous interfaces

The CCl_4/H_2O interface serves as an ideal system for studying liquid diffusion near interfaces. In a static mixture of CCl_4 and H_2O, CCl_4, being denser, settles below the water layer, creating a distinct interface visible to the naked eye. Using the Bessel-like beam as the incident light directed from top to bottom, we recorded the Raman image of the interface region, as shown in FIG. 8(a).

As anticipated, the Raman intensities of the three vibrational peaks exhibit significant variations near the interface (FIG. 8(a)). The intensity distribution along the vertical direction at the 1151 pixel position is plotted in FIG. 8(b), revealing a sigmoid-functional dependence. Obviously, in the region far from the interface, the Raman intensities are consistent with those in bulk-phase CCl_4 and H_2O. The downward trend in Raman intensity with increasing vertical pixels in FIG. 8(b) corresponds to the decrease in CCl_4 density within the interface region.

To better fit the observed intensity distribution, a double Boltzmann sigmoidal function of Eq.(1) is used to fit the variation of the CCl_4 molecular density, as shown in FIG. 8(b),

$$I(x) = I_0 + \frac{A_1}{1+\mathrm{e}^{(x-x_{\mathrm{m}1})/\Delta x_1}} + \frac{A_2}{1+\mathrm{e}^{(x-x_{\mathrm{m}2})/\Delta x_2}} \quad (1)$$

where I_0 is the baseline, A_1 and A_2 are the amplitudes of two components, $x_{\mathrm{m}1}$, $x_{\mathrm{m}2}$ and Δx_1, Δx_2 are the midpoint and half of the transition interval, respectively. The fitting parameters are summarized in Table I.

TABLE I The midpoints (x_{m}), the half intervals (Δx), and the corresponding width (Δd) of transition region for the two components in the double Boltzmann sigmoidal fitting.

Component	x_{m}/pixel	Δx/pixel	$\Delta x'$[a]/pixel	Δd/μm
Slow	143±1.8	49.3±2.5	49.2±2.5	787±40
Fast	135±3.5	4.6±2.2	<2.9[b]	<1 [41]

[a] After the correction of IRF by deconvolution.
[b] The width is smaller than the resolution.

Obviously, the midpoints of the two sigmoidal functions were quite close, while the transition intervals were obviously different, *e.g.* 49.3 and 4.6 pixels. Moreover, the amplitude of the slowly changing component (A_1) is roughly twice as strong as that of the fast component (A_2). Accordingly, three layers are approximately discerned near the boundary as marked with grey and yellow boxes in FIG. 8(b). Notably, the half interval of the fast component is only 4.6 pixels, less than the instrumental resolution (FWHM is 13.4 pixels). Thus, we can expect an approximate step function for its density

DOI: 10.1063/1674-0068/cjcp2502011

distribution, when considering the effect of IRF. This result aligns with the fact that the interfacial layer between CCl_4 and H_2O is only a few nanometers thick through vibrational sum frequency spectroscopy [41]. In contrast, the half interval of the slow component is determined to be 49.3 pixels. After deconvolution with the above Gaussian-function IRF, the variation of the CCl_4 molecular density along the direction can be achieved for the slow component and plotted in FIG. 8(c). As a result, the corresponding width (Δd), defined as $\Delta d = 4 \cdot \Delta x'$, is determined to be 787 μm, implying that as the diffusion distance increases, the CCl_4 molecular number density gradually decreases on the scale of hundreds of micrometers until it reaches homogeneity.

As the variation of molecular density essentially stems from thermal kinetics, at least two factors have comparable effects on the diffusion kinetics on the boundary between CCl_4 and H_2O phases. Therefore, the observed double components in FIG. 8 strongly indicate that the equilibrium between diffusion and deposition in this system is not only affected by thermal motion, but the microstructure due to intermolecular interactions such as hydrogen bonding may also have important influences. These results provide new clues for molecular diffusion thermodynamics and molecular dynamics simulations.

IV. CONCLUSION

In this work, a Bessel-like laser beam was employed in our upgraded Raman spectrometer as the incident illumination. Thanks to the long-depth focus characteristics of the beam, the upgraded system not only remarkably improves the detection sensitivity (detected intensity is increased nearly 6-fold in the same conditions compared with the Gaussian-beam mode), but also significantly suppresses the interferences from the Rayleigh scattering in the low-frequency range.

Moreover, as the detected image of CCD is a projection of the incident illumination region, it makes the spectrometer have another application of recording the Raman images of heterogeneous phase interfaces. A few proof-of-concept experiments have been conducted. The spatial resolution of interface-imaging using the current spectrometer is determined to be 52 microns. Obviously, the resolution is sufficient for the Raman imaging of the liquid-liquid diffusion interface region. Three layers of molecular density have been approximately discerned near the interface of the CCl_4/H_2O system.

Supplementary materials: A schematic diagram of classical 90°-scattered optical system using a Gaussian beam is included (FIG. S1). FIG. S2 shows simulated intensity distribution along an extremely thin interface considering the Gaussian type IRF.

V. NOTES

The authors declare no conflicts of interest.

VI. ACKNOWLEDGMENTS

This work was supported by the National Natural Science Foundation of China (Nos. 22027801, 22073088 and 22473104).

[1] R. Pandey, S. K. Paidi, T. A. Valdez, C. Zhang, N. Spegazzini, R. R. Dasari, and I. Barman, Acc. Chem. Res. **50**, 264 (2017).
[2] K. Q. Wang, Z. L. Li, J. J. Li, and H. Lin, Trends Food Sci. Technol. **118**, 490 (2021).
[3] S. Schlücker, B. Küstner, A. Punge, R. Bonfig, A. Marx, and P. Ströbel, J. Raman Spectrosc. **37**, 719 (2006).
[4] V. O. Baron, M. Z. Chen, S. O. Clark, A. Williams, R. J. H. Hammond, K. Dholakia, and S. H. Gillespie, Sci. Rep. **7**, 9844 (2017).
[5] H. Y. Shen, N. Chen, A. You, Y. Q. Yu, X. G. Zhou, R. Zhang, and S. L. Liu, Chin. J. Chem. Phys. **37**, 763 (2024).
[6] R. Signorell and J. P. Reid, *Fundamentals and Applications in Aerosol Spectroscopy*, Boca Raton: CRC Press, (2010).
[7] J. J. Baraga, M. S. Feld, and R. P. Rava, Appl. Spectrosc. **46**, 187 (1992).
[8] V. Deckert and W. Kiefer, Appl. Spectrosc. **46**, 322 (1992).
[9] J. Durnin, J. J. Miceli, and J. H. Eberly, Phys. Rev. Lett. **58**, 1499 (1987).
[10] M. Fortin, M. Piché, and E. F. Borra, Opt. Express **12**, 5887 (2004).
[11] M. Sakah and B. Chebbi, Opt. Eng. **55**, 091411 (2016).
[12] B. Yalizay, T. Ersoy, B. Soylu, and S. Akturk, Appl. Phys. Lett. **100**, 031104 (2012).
[13] M. K. Bhuyan, M. Somayaji, A. Mermillod-Blondin, F. Bourquard, J. P. Colombier, and R. Stoian, Optica **4**, 951 (2017).
[14] R. D. Davis, S. Lance, J. A. Gordon, and M. A. Tol-

bert, Anal. Chem. **87**, 6186 (2015).
[15] S. R. Lee, J. Kim, S. Lee, Y. Jung, J. K. Kim, and K. Oh, Opt. Express **18**, 25299 (2010).
[16] A. K. Glaser, Y. Chen, and J. T. C. Liu, Optica **3**, 861 (2016).
[17] F. Masia, I. Pope, P. Watson, W. Langbein, and P. Borri, Anal. Chem. **90**, 3775 (2018).
[18] J. X. Lv, C. W. Zhu, Z. Y. Tang, Q. Z. Li, K. Liu, W. Zhang, K. Liu, and X. Y. Li, J. Anal. At. Spectrom. **36**, 2756 (2021).
[19] F. Ren, H. Y. Wang, N. Wang, Y. C. Liu, Y. H. Zhan, and X. L. Chen, *Proceedings of Advanced Chemical Microscopy for Life Science and Translational Medicine*, San Francisco, 112521D (2020).
[20] N. Wang, F. Ren, L. Li, H. Y. Wang, L. Wang, Q. Zeng, Y. L. Song, T. T. Zeng, S. P. Zhu, and X. L. Chen, Biomed. Opt. Express **13**, 2488 (2022).
[21] H. Fleming, M. Z. Chen, G. D. Bruce, and K. Dholakia, Anal. Methods **12**, 4572 (2020).
[22] D. McGloin and K. Dholakia, Contemp. Phys. **46**, 15 (2005).
[23] H. F. Wang, L. P. Shi, B. Lukyanchuk, C. Sheppard, and C. T. Chong, Nat. Photon. **2**, 501 (2008).
[24] M. J. Schultz, S. Baldelli, C. Schnitzer, and D. Simonelli, J. Phys. Chem. B **106**, 5313 (2002).
[25] S. Gopalakrishnan, D. F. Liu, H. C. Allen, M. Kuo, and M. J. Shultz, Chem. Rev. **106**, 1155 (2006).
[26] Y. R. Shen and V. Ostroverkhov, Chem. Rev. **106**, 1140 (2006).
[27] H. F. Wang, W. Gan, R. Lu, Y. Rao, and B. H. Wu, Int. Rev. Phys. Chem. **24**, 191 (2005).
[28] D. R. Dietze and R. A. Mathies, ChemPhysChem **17**, 1224 (2016).
[29] W. Kiefer, J. Raman Spectrosc. **40**, 1766 (2009).
[30] K. Kneipp, H. Kneipp, I. Itzkan, R. R. Dasari, and M. S. Feld, J. Phys.: Condens. Matter **14**, R597 (2002).
[31] A. Otto, I. Mrozek, H. Grabhorn, and W. Akemann, J. Phys.: Condens. Matter **4**, 1143 (1992).
[32] S. Schlücker, Angew. Chem. Int. Ed. **53**, 4756 (2014).
[33] B. Sharma, R. R. Frontiera, A. I. Henry, E. Ringe, and R. P. van Duyne, Mater. Today **15**, 16 (2012).
[34] Z. Q. Tian, B. Ren, and D. Y. Wu, J. Phys. Chem. B **106**, 9463 (2002).
[35] H. P. Liu, H. Su, N. Chen, J. Cen, J. J. Tan, B. C. Zhang, X. Y. Chen, A. Y. Cheng, S. Q. Fu, X. G. Zhou, S. L. Liu, X. P. Zhang, S. Y. Liu, Y. Luo, and G. Q. Zhang, Angew. Chem. Int. Ed. **63**, e202405314 (2024).
[36] D. X. Liu, N. Chen, T. L. Zhang, X. G. Zhou, and S. L. Liu, J. Raman Spectrosc. **55**, 787 (2024).
[37] X. D. Chen, L. Xing, X. F. Li, N. Chen, L. M. Liu, J. H. Wang, X. G. Zhou, and S. L. Liu, ACS Omega **8**, 16439 (2023).
[38] X. F. Li, X. D. Chen, N. Chen, L. M. Liu, X. G. Zhou, and S. L. Liu, Chin. J. Chem. Phys. **36**, 517 (2023).
[39] L. Xing, W. Fan, N. Chen, M. N. Li, X. G. Zhou, and S. L. Liu, J. Raman Spectrosc. **50**, 629 (2019).
[40] W. Fan, L. Xing, N. Chen, X. G. Zhou, Y. Q. Yu, and S. L. Liu, J. Phys. Chem. B **123**, 8057 (2019).
[41] D. S. Walker, F. G. Moore, and G. L. Richmond, J. Phys. Chem. C **111**, 6103 (2007).

DOI: 10.1063/1674-0068/cjcp2502011